WATER SURFACE ALBEDO MODELLING FOR FLOATING PV PLANTS

Shahina S. Patel[1], Arnold J. Rix[2]

Department of Electrical and Electronic Engineering, University of Stellenbosch,

Stellenbosch, 7600, South Africa; +27 61 149 2854; [1] 19480407@sun.ac.za; [2] rix@sun.ac.za

Abstract

Varying albedo, due to water surface, is currently not incorporated in PV yield simulation software. In the absence of measured data of reflected radiation from water, a default albedo value of 0.2 is generally used in the modelling of Floating Photovoltaic (FPV) systems. This paper presents modelling of water surface's varying albedo with the change in the position of the sun; as any weather related changes and reflection off water surface will have a strong impact on the radiation received on the module.

Results shows that the albedo variations are due to the spectral and angular dependencies of the reflective properties and changes of the water surface. Water reflectivity is very low at low incidence angles and it is high only during very early morning and late afternoon when the sun elevation angle is low. The degree of polarisation of light varies throughout the day, so the reflectivity changes at these times and using a default albedo value of 0.2 may underestimate the incident water reflected radiation.

Keywords: floating PV; water surface albedo; reflected radiation; modelling.

1. Introduction

Electricity crisis demands alternative sources of energy generation. Moving away from coal-intensive energy generation allows for production of clean and renewable energy sources. The biggest renewable energy source is the Sun, thus usage of solar energy is the most promising energy providing cost-effective, sustainable and eco-friendly energy alternative to fossil fuels. However, the biggest problem with the implementation of solar energy is the availability of land which is scarce in the world [1]. The burden of ground mounted solar systems is extensively increasing due to shortage of land. Therefore, investigations into alternative forms of production of solar energy is required.

Approximately 71 % of the Earth's surface is water which makes it easier to utilize the concept of solar energy to address the electricity crises through the implementation of floating solar PV (also known as "floatovoltaics") systems. This new ecological alternative solution allows installation of solar PVs over any water bodies [2].

The development of FPV systems and bifacial PV modules on water are two rapidly growing technologies in the PV sector [3], [4]. Since the last decade, floating solar has become a viable market and it is definitely emerging very quickly worldwide with 200+ global floating solar plants to date, June 2019 [5]. Initially, the main objective of floating solar was to make better usage of underutilised or polluted water bodies. However, currently floating solar projects are identified as the key to modifying the world's power supply to more sustainable energy generation.

As Asia dominates the global floating solar projects, the rest of the world continues to follow the trend. Table 1 shows the capacity of the floating solar projects worldwide [5]. In March 2019, the first floating solar PV installation of 59 kW was unveiled in Marlenique, South Africa (SA) [6]. As the floating solar market accelerates, so does Africa gets ready for floating solar making a step towards climate change and sustainable development.

FPV Location	Installed Capacity [kW]
Asia	813 788
Europe	19 915.31
America	1 784
Middle East	1 319.10
Oceania	130
Africa	59

Table 1. Total capacity of FPV projects globally till date

However, practically before installing a FPV system, it is crucial to establish the energy production of the possible deployment of a PV farm. Due to the large investment needed for the installation of an FPV plant, an investor is curious to know how the potential installation of a large-scale floating solar PV plant may benefit the solar energy sector [7]. The main purpose of this paper is to develop a model for estimating the albedo for a smooth water surface.

2. Albedo Effect of Water

Albedo is an dimensionless fraction which is measured from a scale of 0 to 1 with an albedo value of 0 referring to the water surface as a perfectly black surface (perfect absorber) and a albedo value of 1 as a highly reflective surface (perfect reflector) [8]. Albedo of water is the fraction of the incident irradiance that the water surface reflects. The fraction of the sunlight which is not reflected is absorbed by the water surface. The absorbed sunlight then increases the temperature of the water surface, stimulates the evaporation process and energises the heat exchange between air and water.

Figure 1 and 2 demonstrates the albedo effect on a smooth water surface relevant to the solar elevation.

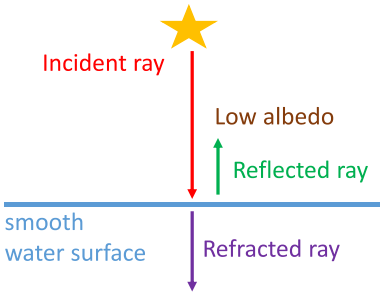

Fig. 1. High solar elevation

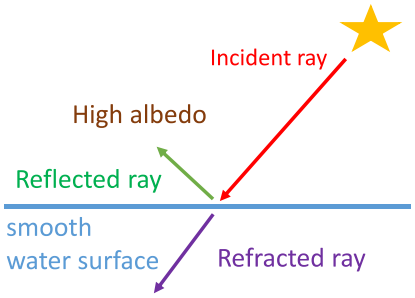

Fig. 2. Low solar elevation

Albedo effect has a significant impact on the climate. The lower the albedo, the more radiation from the sun that gets absorbed by the water, and temperature will rise. When the water albedo is higher, and the water bodies are more reflective, the more radiation is returned to space and also reflected on the rear side of the bifacial module cooling the environment as well as maximizing energy generation from bifacial modules in comparison to mono-facial modules respectively. The aim of bifacial technology on water is to capture more solar energy per module. The albedo effect of water is one of the critical factors which needs to be accounted for in FPV systems as it affects climate change and the uneven heating of the water bodies can drive weather. It is presumed that due to the reflection of irradiation from the water surface, a positive impact can be expected from the installation of FPV on water.

The water reflected radiation from a smooth water surface is estimated using the combination of Fresnel's law and Snell's law [9]. The albedo model is based on specular reflection, i.e. mirror-like reflection as it obeys the law of reflection from a smooth surface at definite angle. The incident light is assumed to be reflected from a "perfectly" smooth water surface in a single direction. The reflectivity of a smooth water surface (still water surface) is calculated using the Fresnel's formula which describe the reflection and transmission of light (or electromagnetic radiation in general) when incident on an interface between different optical media.

Fresnel's law of reflection is expressed as [10]:

$$\theta_1 = \theta_2.$$

With θ_1 and θ_2 as the incident and reflected angles on the water surface normal to the zenith.

Figure 3 demonstrates the interface between air and water.

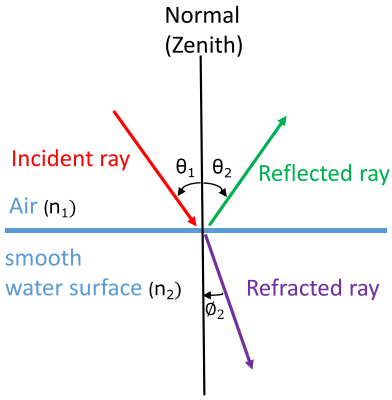

Fig. 3. Interface of the reflected radiation from air to water

Using the Snell's law of refraction, the refracted angle (transmitted angle) is computed as follows [11]:

$$\emptyset_2 = \sin^{-1}\frac{n_1 \cdot sin(\theta_1)}{n_2}.$$

With n_1 and n_2 the refractive index of air and water medium respectively.

3. Modelling

3.1 Clear Sky Models

In lieu of measurements, identifying relevant clear sky models to predict the daylight quantities is a crucial step in developing the albedo model. The two clear sky models which are available in pvlib-python are Ineichen and Perez [12] and the Simplified Solis [13]. Therefore, these two models are implemented to

predict the incoming solar radiation and are compared respectively to the measured irradiance, i.e. Global Horizontal Irradiance (GHI), Direct Normal Irradiance (DNI) and Diffuse Horizontal Irradiance (DHI). Comprehensive validation of the model accuracy are assessed using the relative performance matrices i.e. Mean Bias Error (MBE) and Root Mean Square Error (RMSE).

The measured data is acquired from a data logger which is connected to a range of high quality solar and weather sensors at the rooftop of civil engineering building of Stellenbosch University, South Africa. Minutely weather data is recorded from 01 January 2018 till 31 December 2018. The annual data is analysed and cleaned; and the most clear sky day is then obtained for each of the seasons, i.e. summer, spring, autumn and winter.

Parameters of the location are as follows:

Latitude = -33.927905°,
Local longitude = 18.865266°,
Local time meridian = 30.0°.

3.1.1 Simplified Solis

The Simplified Solis model parameterises the clear sky GHI, DNI, and DHI in terms of the Aerosol Optical Depth (AOD) and precipitable water. Precipitable water value ranges from 0.2 - 10 cm [14]. However, for this model, the default value used in the pvlib-python software is 1 [15]. It is used with the assumption that all the water vapour in a vertical column of air is condensed into liquid water. The Simplified Solis is approximated by a single broadband of AOD at a wavelength at 700 nm [14]. AOD is a dimensionless number which measures how much direct sunlight is prevented from reaching the water surface due to aerosol particles such as dust and haze.

After evaluation of the measured irradiance data with the modelled Simplified Solis irradiance, the AOD value was adjusted accordingly for accurate approximation of the clear sky days. It was found that in Stellenbosch the AOD ranges between 0.049 and 0.117 as shown in Table 2.

3.1.2 Ineichen and Perez

The Ineichen-Perez model parameterises the clear sky GHI, DNI, and DHI in terms of the Linke turbidity. The Linke turbidity factor is a very suitable approximation used to model the solar irradiance, atmospheric absorption and scattering under clear skies [16].

Table 2 shows the Linke turbidity factor which is adjusted accordingly to best fit the measured data and the clear sky model data.

Seasons	AOD	Linke turbidity
Summer	0.117	0.848
Autumn	0.049	1.102
Winter	0.056	0.635
Spring	0.069	1.425

Table 2. Seasonal variation of AOD and Linke turbidity in Stellenbosch

3.2 Clear Sky Model Verification

For accurate performance prediction of FPV systems, it is essential that the solar irradiance are precisely matched with the measured real-time data. Clear sky estimates from the two clear sky models were computed and compared to the measured irradiance for each of the clear sky days of the seasons using the two error matrices as shown [17].

$$MBE = \frac{1}{N}\sum_{i=1}^{N}(\hat{y} - y_m),$$

$$RMSE = \sqrt{\frac{1}{N}\sum_{i=1}^{N}(\hat{y} - y_m)^2},$$

Table 3 and 4 shows how the GHI components computed error matrices for the two clear sky models varies seasonally.

Seasons	RMSE [W/m^2]	MBE [W/m^2]
Summer	7.18	-0.23
Autumn	3.85	-0.19
Winter	4.45	0.02
Spring	5.86	-0.14

Table 3. Ineichen-Perez modelled and measured GHI comparison

Seasons	RMSE [W/m^2]	MBE [W/m^2]
Summer	9.18	0.15
Autumn	3.84	0.24
Winter	6.06	0.60
Spring	5.56	0.35

Table 4. Simplified Solis modelled and measured GHI comparison

The variation in the errors between the two clear sky models are dependent on the attenuation of the Linke turbidity factor and AOD. Both clear sky model errors are acceptable within the ranges obtained [18], [19]. Therefore, the range of the errors of

the two clear sky models shows that both the models are a good estimate for predicting the solar radiation. However, due to minimal input data set for each of the days, the Ineichen and Perez model is used in this paper for predicting the irradiance.

Figure 4 shows the measured GHI on a clear sky day in summer and the modelled GHI component of the two clear sky models.

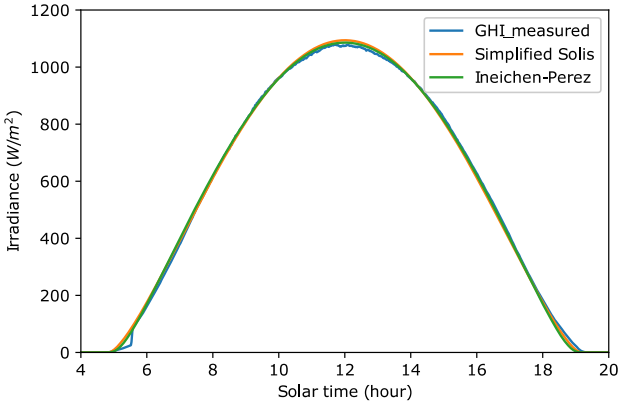

Fig. 4. Measured GHI and clear sky model

3.3 Optics at an Air-Water Interface

In optics, any media in which light can propagate has an index of refraction, denoted by *n* and is dimensionless defined as:

$$n = \frac{c}{v} = \frac{c/f_1}{v/f_2} = \frac{\lambda_0}{\lambda}.$$

With c the speed of light in vacuum, v the phase velocity of light in the medium, λ_0 and λ as the wavelength in vacuum and medium respectively, f_1 and f_2 as the frequency which remains equal as light waves travel from air to water and vice versa [20]. The refractive indices is a key factor which needs to be accounted for when modelling the albedo of water. To obtain the values of the indices, there are two suitable techniques. Using a refractometer, the index can be measured directly or by using specific sensors to measure the atmospheric pressure, humidity and air temperature. Therefore, in the absence of measured data of the indices, a precise estimation of the refractive index of air and water is computed using the Edlén's and Lorentz-Lorenz equation respectively.

3.3.1 Index of Refraction of Air

The refractive index for dry air n_{Air} is specified to be at 15 ℃ with a pressure of 101.325 kPa containing 0.045 % volume of CO_2, i.e. standard air [21]. The index of refraction of air is defined as the ratio of the wavelength of the radiation in the air with reference to a vacuum, therefore [20]:

$$n_{air} = \frac{\lambda_{vac}}{\lambda_{air}}.$$

The index of refraction is computed as a function of the wavelength using the following expression of the modified Edlén's equation [21]:

$$(n_{air} - 1) \cdot 10^8 = 8342.54 + 2406147(130 - \sigma^2)^{-1} + 15998(38.9 - \sigma^2)^{-1}.$$

Whereby $\sigma = \frac{1}{\lambda_{vac}}$ with λ_{vac} in units of μm ranging from 200 nm to 1100 nm.

However, for effective approximation of the refractive index of air, it is computed at a varying temperature T in ℃ ranging from 0 ℃ to 100 ℃ and a pressure p in Pascal. Therefore, the value of $(n_{air} - 1)$ is multiplied by the following expression [20]:

$$n_{air}(T,p) = (n_{air} - 1)\left(\frac{p[1 + p(60.1 - 0.972t)\cdot 10^{-10}]}{96095.43(1 + 0.003661T)}\right) + 1.$$

Figure 5 shows how the refractive index of air decreases with an increase in wavelength and temperature.

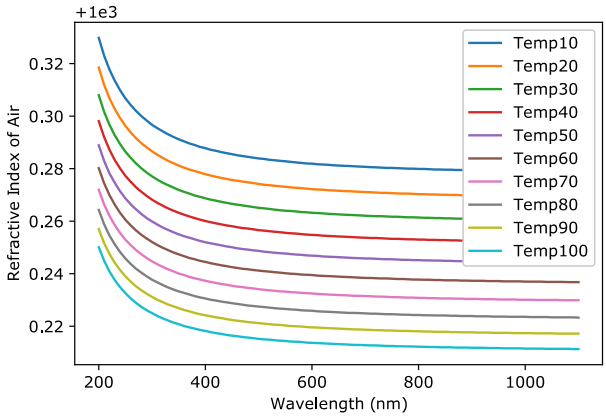

Fig. 5. The variation of refractive index of air with wavelength for various temperatures

3.3.2 Index of Refraction of Water

The refractive index of liquid water n_{water} is computed at atmospheric pressure, relative to a vacuum which covers a range of wavelength, temperature, and density. The Lorentz-Lorenz function (molar refraction) is used as a foundation to compute the index of refraction of water and is defined as [22]:

$$LL = \frac{{n_{water}}^2 - 1}{({n_{water}}^2 + 2)p_m} = \frac{N_A \alpha}{3\varepsilon_0}.$$

With p_m the liquid water density in moles per unit volume, N_A is Avogadro's number, α the molecular polarisability at optical frequencies and ε_0 the permittivity of vacuum.

However, to determine the dependency of wavelength on the molar refraction, the dispersion relation is used as [22]:

$$LL = a_0 + \sum_i \frac{a_i}{\lambda^2 - \lambda_i^2}.$$

With a_i the resonance strength constants and λ_i the wavelength related to the i^{th} resonance. Although the Lorentz-Lorenz function covers all the resonances, for this formulation the effective infrared and ultraviolet resonances are of interest as it is presumed to have a prevailing effect on the refractive index as [22]:

$$LL = a_0 + \frac{a_{IR}}{\lambda^2 - \lambda_{IR}^2} + \frac{a_{UV}}{\lambda^2 - \lambda_{UV}^2}.$$

With least square adjustments of a_0, a_{IR} and a_{UV} and selective λ_{IR} and λ_{UV}, the modified formulation of Lorentz-Lorenz function provides more accurate refractive index data in the visible spectrum.

Furthermore, the formulation is expanded to relate the variation of temperature, density and wavelength dependency of the Lorentz-Lorenz function of liquid water as [22]:

$$\frac{{n_{water}}^2 - 1}{({n_{water}}^2 + 2)p^*} = a_0 + a_1 p^* + a_2 T^* + a_3 \lambda^{*2} T^* + \frac{a_4}{\lambda^{*2}} + \frac{a_5}{\lambda^{*2} - \lambda_{UV}^{*2}} + \frac{a_6}{\lambda^{*2} - \lambda_{IR}^{*2}} + a_7 p^{*2}.$$

Whereby,

$$p^* = \frac{p}{p_0}; \qquad p_0 = 1000\ kg.m^{-3},$$
$$T^* = \frac{T}{T_0}; \qquad T_0 = 273.15\ K,$$
$$\lambda^* = \frac{\lambda}{\lambda_0}; \qquad \lambda_0 = 0.589\ \mu m.$$

With p the density, T the absolute temperature and λ the wavelength. The dependency of the independent variables ranges are as follows:

$$T < 100\ ℃,$$

$$\lambda < 1100\ nm,$$

$$p < 999.84\ kg.m^{-3}.$$

The coefficients a_0 to a_7, λ_{UV} and λ_{IR} are selectively optimised to fit the data range and are given in Table 5 [22].

Coefficients	Value
a_0	0.243905091
a_1	9.53518094e-3
a_2	-3.64358110e-3
a_3	2.65666426e-4
a_4	1.59189325e-3
a_5	2.45733798e-3
a_6	0.897478251
a_7	-1.63066183e-2
λ_{UV}^*	0.2292020
λ_{IR}^*	5.432937

Table 5. Lorentz-Lorenz function

Figure 6 shows how the refractive index of water decreases with an increase in wavelength and temperature.

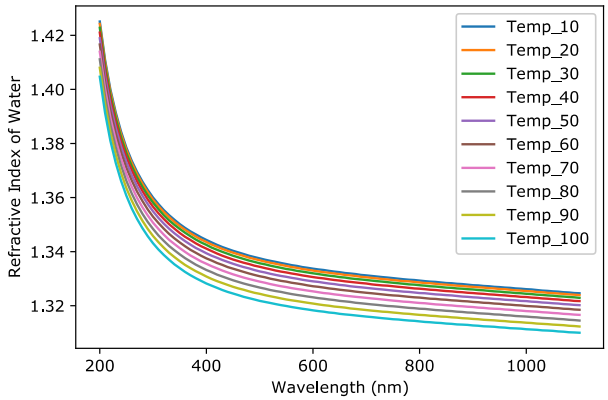

Fig. 6. The variation of refractive index of water with wavelength for various temperatures

3.4 Albedo approximation

In this paper, the albedo model is approximated based on the assumption that the incident ray of light which strikes the water surface is the DNI component. DNI on a clear sky day is most prominent and the clear sky model provides a more accurate forecast. When the incident light ray encounters at the interface of the water surface, some of the light is reflected off the water surface while the remaining is transmitted through the liquid water.

Sunlight from the Sun is a transverse wave therefore the albedo model also assumes that the incoming incident light which strike the water surface is unpolarised which means that the electric fields from the radiation oscillates in all directions consisting of two orthogonal linear s and p polarisation with equal amplitude and phase difference of 90 ° [23]. For reflection and transmission of light, s and p polarised light are defined as lights which has electric fields oriented perpendicular to the plane of incident and parallel to that plane respectively.

The reflection coefficient for both the parallel and perpendicular polarised light are expressed as a function of the incident angle θ_i and transmitted angle θ_t as follows [24]:

$$r_{\parallel} = \frac{tan^2(\theta_i - \theta_t)}{tan^2(\theta_i + \theta_t)},$$

$$r_{\perp} = \frac{sin^2(\theta_i - \theta_t)}{sin^2(\theta_i + \theta_t)}.$$

The total unpolarised light reflection coefficient R_u is then determined by [23]:

$$\mathrm{R_u} = \frac{(r_{\parallel} + r_{\perp})}{2}.$$

The transmission coefficient is calculated as [23]:

$$T = 1 - \mathrm{R_u}.$$

Once the incident light enters the surface of the water medium, the refracted and reflected rays become polarised and partially polarised depending on the angles at which the rays are striking off. Other internal reflections in the water surface are also neglected in this model.

Furthermore, the incident angle is equivalent to the solar zenith angle ($\theta_i = \theta_z$) and is defined as the angle between the zenith (normal to the centre of earth) and the centre of the Sun. The solar zenith angle is expressed as [25]:

$$\theta_z = 90° - \beta.$$

With β the solar elevation angle (altitude angle). The solar elevation angle is computed as follows [25]:

$$\sin\beta = (\cos L \cdot \cos\delta \cdot \cos H) + (\sin L \cdot \sin\delta).$$

With L the latitude of the respective location, H the hour angle, and δ the declination angle.

4. Modelling results

Figure 7 shows the Fresnel's effective smooth water surface reflectance and transmission coefficient of *s* and *p* polarization of radiation at various angles of incident for the 200nm wavelength. The green (T_s) and red (T_p) curves are the transmission coefficient of the transmitted waves of the *s* and *p* polarization of radiation respectively. While the blue (R_s) and orange (R_p) curves are the reflection coefficient of the reflected waves of the *s* and *p* polarization of radiation respectively. It is observed that for angle of incidence less than 70°, higher amounts of light is transmitted than reflected. However, as the angle of incident reaches 90°, also called the grazing incident, all the light is reflected.

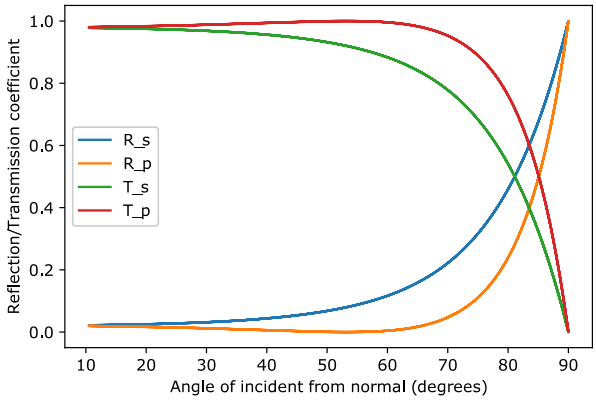

Fig. 7. Fresnel's external reflection off smooth water surface

Contrary to a common belief that FPV can benefit from high reflection from water surfaces [26], the overall albedo on the water surface is actually quite low. Figure 8 shows that the commonly used default albedo value of 0.2 is a far offset estimate and is unreliable, and is advised not to be used in the modelling of FPV systems. Therefore, the albedo model developed in this paper shows a more accurate presentation of the effect of albedo from a smooth water surface.

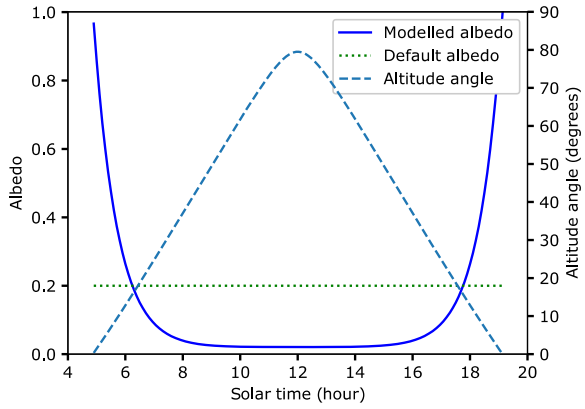

Fig. 8. Albedo model on a clear sky summer solstice

Figures 9 to 11 shows the variation of albedo on a very sunny clear sky day for the four seasons respectively. The clear sky day's albedo is modelled for a wavelength of 500 nm in the visible spectrum. The albedo effect on the clear sky days illustrates that the reflected radiation is high during sunrise and sunset only. This is due to the lower solar elevation observed during sunrise and sunset, resulting in the higher albedo values.

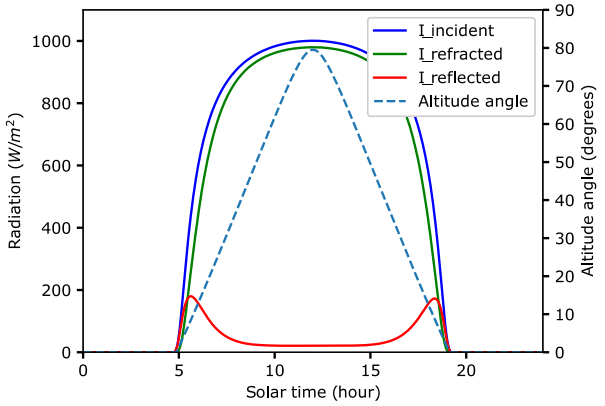

Fig. 9. Albedo effect on a clear sky summer solstice

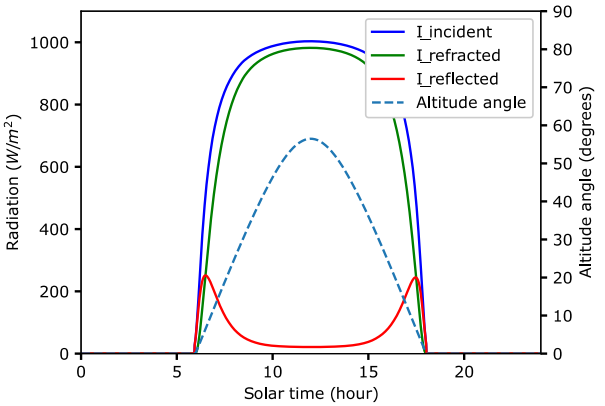

Fig. 10. Albedo effect on a clear sky spring/autumn equinox

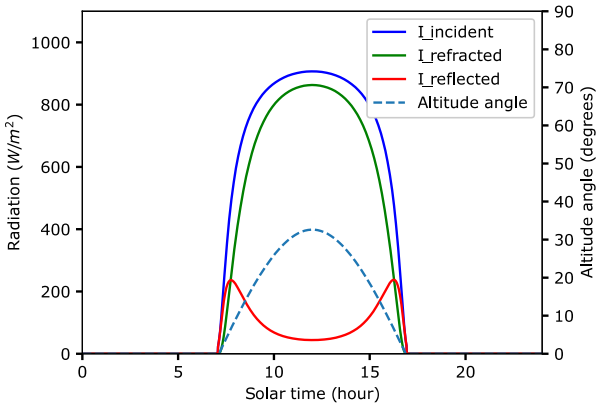

Fig. 11. Albedo effect on a clear sky winter solstice

Figure 12 shows how the albedo varies due to the wavelength variation on a clear sky September equinox. It is observed that the overall albedo increases with a decrease in wavelength and that the albedo's dependence on the temperature is insignificant.

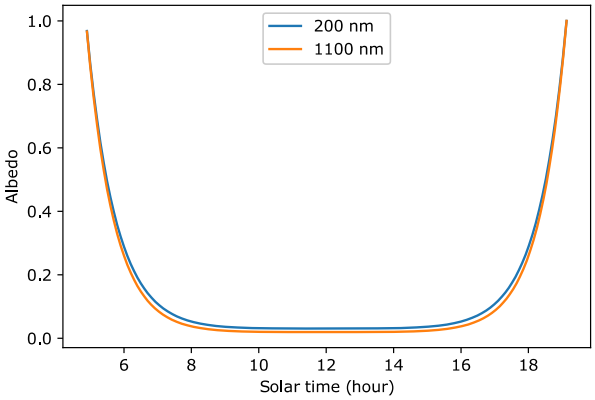

Fig. 12. Albedo at different wavelength

At a constant wavelength and temperature of 500 nm and 15 ℃ respectively, the effect of the wavelength and temperature variation is evaluated for each of the seasons. It is found that for all the seasons the effect of temperature variation is very minimal with an albedo difference of 1 % between the minimum and the maximum temperature of 10 ℃ and 100 ℃. The albedo difference due to the wavelength variation between the minimum and the maximum wavelength of 200 nm and 1100 nm is found to be 3 % for all the seasons.

5. Conclusion

In this paper the albedo of a flat water surface as a function of time, temperature and wavelength is calculated. The time varying component of albedo is influenced by the position of the sun and this together with the intensity of DNI is accounted for by using the Simplified Solis and Ineichen-Perez clear sky models. Combining the position of the Sun with Fresnel's and Snell's laws the reflection and refraction of water can be calculated. The refraction index of air and water is however influenced by temperature and wavelength.

Results shows that the albedo of a smooth water surface is not constant and the results illustrates that temperature and wavelength are not the critical factors which affects the albedo but rather the position of the Sun. Early morning and late afternoon, when radiation intensity is low, high albedo values are observed. During the middle of the day, the albedo value is much lower than the default value of 0.2 which is typically used. Lower water surface albedo will therefore also result in lower bifacial module performance gain when used on open water surfaces.

Acknowledgement

The author, Ms Patel would like to convey her gratitude to Scatec Solar for supporting her master's degree programme.

References

[1] Kim, S., Oh, M. and Park, H. (2019). Analysis and Prioritization of the Floating Photovoltaic System Potential for Reservoirs in Korea. *Applied Sciences*, 9(3), p.395.

[2] Liu, H., Krishna, V., Lun Leung, J., Reindl, T. and Zhao, L. (2018). Field experience and performance analysis of floating PV technologies in the tropics. *Progress in Photovoltaics: Research and Applications*, 26(12), pp.957-967.

[3] Kreiter, R. (2019). *Floating bifacials Reflections on power*. [online] Bifipv-workshop.com. Available at: http://bifipv-workshop.com/fileadmin/layout/images/Konstanz-2017/6__R._Kreiter_SUNFLOAT_Floating_bifacials.pdf [Accessed 5 Sep. 2019].

[4] Etxebarria, J. (n.d.). *Toolbox for the design and simulation of a foating bifacial PV plant with refectors*. [online] Repository.tudelft.nl. Available at: https://repository.tudelft.nl/islandora/object/uuid:a86fd44c-379c-48f8-a737-2c0b01086384/datastream/OBJ/download [Accessed 5 Sep. 2019].

[5] Floating Solar Conference. (2019). *200+ Global Floating Solar Plants — Floating Solar Conference*. [online] Available at: https://www.floatingsolarconference.com/news-source/2019/6/5/120-global-floating-solar-plants [Accessed 27 Aug. 2019].

[6] Ciel et Terre International. (2019). *MARLENIQUE FARM: 59 kWp - Ciel et Terre International*. [online] Available at: https://www.ciel-et-terre.net/project/marlenique-farm-59-kwp/ [Accessed 1 Sep. 2019].

[7] Durković, V. and Đurišić, Ž. (2017). Analysis of the Potential for Use of Floating PV Power Plant on the Skadar Lake for Electricity Supply of Aluminium Plant in Montenegro. *Energies*, 10(10), p.1505.

[8] Gul, M., Kotak, Y., Muneer, T. and Ivanova, S. (2018). Enhancement of Albedo for Solar Energy Gain with Particular Emphasis on Overcast Skies. *Energies*, 11(11), p.2881.

[9] Dupertuis, M., Acklin, B. and Proctor, M. (1994). Generalization of complex Snell–Descartes and Fresnel laws. *Journal of the Optical Society of America A*, 11(3), p.1159.

[10] Pickering, E. (1873). Applications of Fresnel's Formula for the Reflection of Light. *Proceedings of the American Academy of Arts and Sciences*, 9, p.1.

[11] Bryant, F. (1958). Snell's Law of Refraction. *Physics Bulletin*, 9(12), pp.317-317.

[12] Perez, R., Ineichen, P., Seals, R., Michalsky, J. and Stewart, R. (1990). Modeling daylight availability and irradiance components from direct and global irradiance. *Solar Energy*, 44(5), pp.271-289.

[13] Ineichen, P. (2008). A broadband simplified version of the Solis clear sky model. *Solar Energy*, 82(8), pp.758-762.

[14] Pvlib-python.readthedocs.io. (2019). *pvlib.clearsky — pvlib-python 0.6.3+18.ga873462.dirty documentation*. [online] Available at: https://pvlib-python.readthedocs.io/en/latest/_modules/pvlib/clearsky.html#simplified_solis [Accessed 5 Sep. 2019].

[15] Molineaux, B., Ineichen, P. and O'Neill, N. (1998). Equivalence of pyrheliometric and monochromatic aerosol optical depths at a single key wavelength. *Applied Optics*, 37(30), p.7008.

[16] Ineichen, P. and Perez, R. (2002). A new airmass independent formulation for the Linke turbidity coefficient. *Solar Energy*, 73(3), pp.151-157.

[17] Badescu, V. (1997). Verification of some very simple clear and cloudy sky models to evaluate global solar irradiance. *Solar Energy*, 61(4), pp.251-264.

[18] Laguarda, A. and Abal, G. (2017). *Clear-Sky Broadband Irradiance: First Model Assessment in Uruguay*.

[19] Ineichen, P. (2006). Comparison of eight clear sky broadband models against 16 independent data banks. *Solar Energy*, 80(4), pp.468-478.

[20] Ciddor, P. and Hill, R. (1999). Refractive index of air 2 Group index. *Applied Optics*, 38(9), p.1663.

[21] Birch, K. and Downs, M. (1993). An Updated Edlén Equation for the Refractive Index of Air. *Metrologia*, 30(3), pp.155-162.

[22] Schiebener, P., Straub, J., Levelt Sengers, J. and Gallagher, J. (1990). Refractive index of water and steam as function of wavelength, temperature and density. *Journal of Physical and Chemical Reference Data*, 19(3), pp.677-717.

[23] Shevchenko, A., Roussey, M., Friberg, A. and Setälä, T. (2017). Polarization time of unpolarized light. *Optica*, 4(1), p.64.

[24] Islam, M., Younis, M. and Ahmed, A. (2018). Communication through Air Water Interface Using Multiple Light Sources. [online] Available at: https://ieeexplore.ieee.org/abstract/document/8422432/authors#authors [Accessed 28 Aug. 2019].

[25] Duffie, J. and Beckman, W. (2013). *Solar engineering of thermal processes*. Hoboken, NJ: John Wiley

[26] Choi, Y. (2014). A Study on Power Generation Analysis of Floating PV System Considering Environmental Impact. *International Journal of Software Engineering and Its Applications*, 8(1), pp.75-84.